1998

Steady-State Modeling of a Parallel-Plate Electrochemical Fluorination Reactor

Kamal Jha
University of South Carolina - Columbia

Gerald L. Bauer

John W. Weidner
University of South Carolina - Columbia, weidner@engr.sc.edu

Publication Info

Journal of the Electrochemical Society, 1998, pages 3521-3530.

Publisher's link: http://dx.doi.org/10.1149/1.1838837
DOI: 10.1149/1.1838837

Steady-State Modeling of a Parallel-Plate Electrochemical Fluorination Reactor

Kamal Jha,*[a] Gerald L. Bauer,[b] and John W. Weidner[a]**

[a]*Center for Electrochemical Engineering, Department of Chemical Engineering, University of South Carolina, Columbia, South Carolina 29208, USA*
[b]*3M Chemicals, St. Paul, Minnesota 55144-1000, USA*

ABSTRACT

A steady-state mathematical model of a parallel-plate reactor was developed for studying the electrochemical fluorination of organic compounds dissolved in anhydrous hydrogen fluoride. The model incorporates two-phase flow with differential material, energy, and pressure balances. Profiles of temperature, pressure, vapor volume fraction, and current density in the reactor are presented at two inlet temperatures to provide insight into the operation of the reactor. The effects of the inlet temperature, feed flow rate, and cell current on the cell pack voltage and current efficiency of the reactor are presented to determine problematic operating regions for the reactor. Optimum operating currents based on the ratio of the moles of fluorochemical produced to the input energy are also calculated.

Introduction

Electrochemical fluorination is used to produce fluorochemicals for use as refrigerants, lubricants, surfactants, degreasers, heat-transfer fluids, high-performance plastics, elastomers, and ingredients for fire fighting foam and fabric protectors. The feed to an electrochemical fluorination reactor is composed of liquid anhydrous hydrogen fluoride and a fluorinatable organic compound. The fluorochemical is produced at the anode and hydrogen gas at the cathode. Some of the hydrogen is reoxidized at the anode, thus adding an inefficiency to the process. In addition, the production of hydrogen results in the development of a two-phase system.

An undivided monopolar series arrangement of nickel electrodes, known as the Simons electrochemical fluorination cell,[1] is the most common reactor design for the fluorination process. Nickel electrodes are used due to their compatibility with anhydrous hydrogen fluoride and good electrochemical activity. The industrial Simons cell operates at high currents (>10,000 A) and requires the use of heavy-duty, high-cost electrical conductors and bus work. The large amount of resistive heating in the cell bus-bars limits the operating current and, therefore, the production rate. Also, the cells rely on bubble generation for the circulation of the electrolyte. The dependence on natural convection leads to slow mass transfer of the reactants to the electrode surface, which increases the cell-pack voltages.

To solve the problems encountered in the Simons cell, a multicell pack with forced convective flow was designed.[2] A schematic of the fluorination reactor simulated in this study is shown in Fig. 1. The reactor considered here has a cell pack consisting of 27 nickel plates, which results in 26 undivided cells. The cells are connected in parallel to the electrolyte flow field and in series (i.e., bipolar) to the electrical circuit. Each of the cells in the cell pack has inlet and outlet flow distributors to provide uniform electrolyte flow. The distributors also act as physical separators between the electrodes and are made of a fluoride resistant, insulating material to reduce shunt current losses. The process is operated above ambient pressure and temperature to increase the yield and decrease the power input.

Although the bipolar, forced flow design reduces energy costs and increases production rates, compared to the Simons process, a better understanding of the process is needed to minimize operational problems and maximize production rates. A steady-state mathematical model of the bipolar fluorination process is developed in this work. The model incorporates two-phase flow with differential material, energy, and pressure balances. The model predictions are compared to the available data over a wide range of operating conditions to test the validity of the model assumptions. Profiles of temperature, pressure, vapor volume fraction, and current density in the fluorination reactor are presented at two inlet temperatures to provide insight into the operation of the reactor. In addition, the dependence of the cell-pack voltage and current efficiency on the inlet temperature, electrolyte flow rate, and cell current are shown to provide insight into the trade-off between power requirements, production rates, and controllability of the reactor.

This paper extends our previous work[3] and contains three features which are not present in a similar modeling effort by Drake et al.[4] First, our model is capable of using either current or voltage as the controlled variable compared to voltage only. Second, the model presented here accounts for the interaction between the cell pack and the other sections of the fluorination reactor (e.g., inlet and outlet flow distributors). These interactions are important in understanding the overall reactor performance and identify-

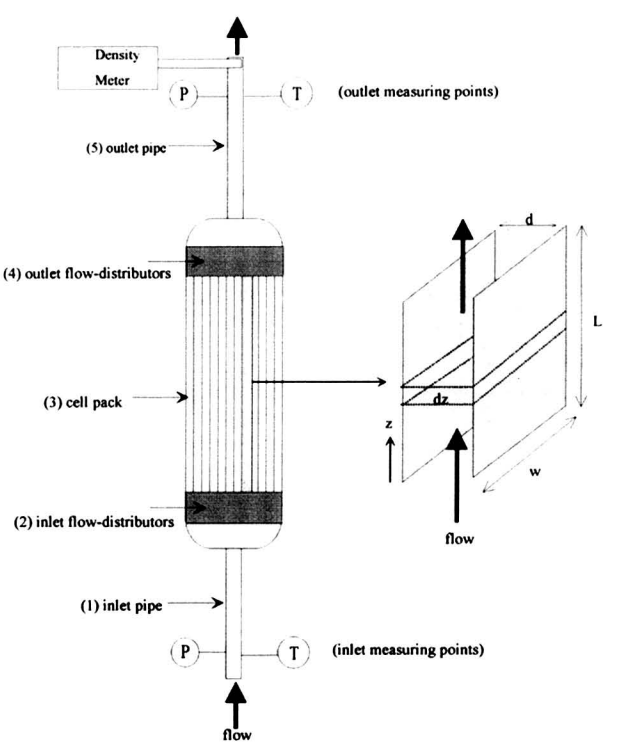

Fig. 1. Schematic diagram of the electrochemical fluorination reactor. The inlet and outlet measurement points for temperature, pressure, and density are indicated on the schematic. A magnified view of one of the parallel-plate cells is also shown.

* Electrochemical Society Student Member.
** Electrochemical Society Active Member.

ing potential operational problems. Third, the hydrogen oxidation reaction is included in order to predict the current efficiency as a function of operating conditions.

Model

Description of the fluorination reactor.—The fluorination reactor (see Fig. 1) is comprised of five sections: (1) inlet pipe, (2) inlet flow distributors, (3) cell pack, (4) outlet flow distributors, and (5) outlet pipe. The cell pack consists of 26 identical parallel-plate cells, and each cell has 18 inlet and outlet flow distributors. The flow distributors are narrow flow channels evenly spaced across the width of each cell, providing uniform flow to all the cells in the cell pack. The following reactions occur at the cathode and anode of each parallel-plate cell in the reactor

Cathode

$$2H^+ + 2e^- \rightarrow H_2$$

Anode

$$RH + 2F^- \rightarrow RF + HF + 2e^-$$

$$H_2 \rightarrow 2H^+ + 2e^-$$

where RF is the fluorinated organic compound, HF is anhydrous liquid hydrogen fluoride, and RH is the fluorinatable organic compound. Due to the use of an undivided cell, some of the hydrogen produced at the cathode is transported to, and oxidized at, the anode. Therefore, the current efficiency of the process, defined as current efficiency of the fluorochemical (RF) production reaction, is less than unity. The overall reaction for the fluorination process can be represented as

$$RH + HF \rightarrow RF + H_2$$

Assumptions.—The assumptions used in the modeling of all the reactor sections are listed below

1. The physical properties of the fluorinatable organic compounds (RH) approximate those of HF in both the liquid and vapor phases. Therefore, the HF/RH mixture is modeled as a single component, which is the dominant species in the liquid phase. Also, the feed to the reactor is completely liquid.
2. Hydrogen fluoride in the vapor phase is treated as an oligomerized molecule with a mean molecular weight of 60 for the range of operating conditions used in this study.
3. The heat capacities of liquid HF and hydrogen are constant in the temperature range under study.
4. The ideal-gas law is valid.
5. No slip occurs between the vapor and liquid phases, which form a homogeneous two-phase mixture due to the bubbly flow regime present in most of the sections of the reactor.
6. The enthalpy of mixing is negligible for both the liquid and vapor phases.
7. The dependent variables vary only in the axial direction, and all the 26 undivided parallel-plate cells behave identically.
8. Heat loss to the surroundings is negligible in all the fluorination reactor sections.
9. The ratio of hydrogen supersaturation to saturation in HF is assumed to be independent of temperature. The temperature dependence of the dissolved hydrogen concentration is obtained through the Henry's law constant.
10. Due to low solubility of hydrogen in the liquid phase,[6] the number of moles of hydrogen in the liquid phase is negligible compared to those in the vapor phase.
11. Oxidation of hydrogen at the anode is mass-transfer limited with a constant mass-transfer resistance caused by an anodic film.
12. The parallel-plate electrodes are equipotential surfaces.

The mean molecular weight of the oligomerized hydrogen fluoride was found by weighting the molecular weight of each HF polymer species by their individual vapor-phase mole fractions. The mole fractions as a function of temperature were obtained from the equilibrium constants for the association of HF to dimers, tetramers, hexamers, and octamers given by Schotte et al.[5] The mean molecular weight of HF in the vapor phase was found to be approximately 60 ± 3 over the temperature range of 25 to 35°C. This mean molecular weight corresponds to that of HF trimer ($n \cong 3$), although the proportion of HF existing as a trimer is insignificant.

No slip, homogeneous flow should be valid as the two-phase flow remains in the bubbly flow regime over the range of normal reactor operation.[7] Although the work by Ali et al.[7] was for the air-water system, their flow regime graphs should provide a conservative guide for this vapor-liquid system. HF electrolyte has a similar density and viscosity to that of water, but the surface tension is approximately ten times less (~6 mN/m for HF and ~70 mN/m for water). The lower surface tension of HF leads to smaller bubbles,[8] which results in more bubbly flow. Therefore, less slip between the vapor and liquid phases should occur at a given vapor fraction. During normal operation of the reactor, the vapor fraction in the cell remains below 0.6. For these values of vapor volume fraction, the no-slip assumption has been used successfully in papers by Funk and Thorpe,[9] Nishiki et al.,[10] and Yan et al.[11] for air-water systems. Therefore, the no-slip assumption should be valid for vapor fractions less than 0.6, and it is most likely valid for values greater than 0.6.

Assumption 8 is valid because the reactor is well insulated and each cell is assumed to be identical (see assumption 7). Since each cell is at the same temperature, there is no driving force for energy exchange between the cells.

The dissolved hydrogen concentration in the HF electrolyte may be supersaturated as is found for gases in other gas evolving systems.[12] Although the degree of supersaturation for hydrogen in HF is not known, the ratio of supersaturation to saturation can be lumped into the mass-transfer coefficient for hydrogen across the anodic film. Therefore, the Henry's law constant can be used to obtain the temperature dependence for dissolved hydrogen (see assumption 9).

Molar balance.—The two-phase system is composed of three species: (*i*) hydrogen; (*ii*) hydrogen fluoride, which includes the fluorinatable organic compound; and (*iii*) the fluorochemical. Eight equations are needed to account for the mole fractions of the three components and the total flow rates of each phase. However, tracking the small amount of fluorochemical in the liquid phase is unnecessary, and therefore, its concentration is set to zero. Therefore, only seven equations are needed to calculate the composition and flow rates throughout the reactor at a particular temperature, pressure, and current. These equations consist of two mole balances, three equilibrium expressions, and two mole-fraction constraints.

Due to no net change in moles in the overall reaction, a steady-state overall mole balance is written as

$$0 = \frac{d\dot{N}}{dz} \quad [1]$$

The molar flux, $\dot{N}$, is constant according to Eq. 1, and is equal to $Q\rho_{m,l}/A_{flow}$). The flux at each point in the reactor is related to the local average molar density (ρ_m) and the no-slip velocity (v) of the two-phase stream as follows

$$\dot{N} = \rho_m v \quad [2]$$

The average molar density (ρ_m) is related to the mole fractions and molar densities of the individual phases by the following equation due to homogeneity of the two-phase mixture (see assumption 5)

$$\frac{1}{\rho_m} = \frac{x_v}{\rho_{m,v}} + \frac{x_l}{\rho_{m,l}} \quad [3]$$

For an ideal gas, the molar density of the vapor phase is related to the pressure and temperature by

$$\rho_{m,v} = \frac{P}{RT} \quad [4]$$

The molar density of the liquid phase is given by

$$\rho_{m,l} = \frac{\rho_l}{MW_l} \quad [5]$$

where the liquid mass density, ρ_l, is a constant and is given in Table III. The molecular weight of HF in the liquid, MW_l, is set equal to 60. The model results are insensitive to the value of MW_l used.

A steady-state balance on hydrogen relates the gradient in the hydrogen molar flux to the net production of hydrogen from the electrochemical reaction by the following equation

$$\frac{d\bar{N}_{H_2}}{dz} = \frac{i - i_{H_2,a}}{nFd} \quad [6]$$

Using assumption 10, the molar flux of hydrogen is related to the total molar flow rate of the two-phase stream, the mole fraction of the vapor phase, and the mole fraction of hydrogen in the vapor phase as follows

$$\dot{N}_{H_2} = y_{H_2} x_v \dot{N} \quad [7]$$

The term on the right in Eq. 6 is composed of the cell current density, i, which determines the generation rate of hydrogen at the cathode, and the hydrogen oxidation current density, $i_{H_2,a}$, which determines its consumption at the anode.

The oxidation of hydrogen at the anode is a result of the undivided cell configuration. Using assumption 11, the oxidation current can be expressed as a function of the mass-transfer coefficient and the mole fraction of dissolved hydrogen as follows

$$i_{H_2,a} = nFk_m x_{H_2} \rho_{m,l} \quad [8]$$

It is necessary to relate the dissolved hydrogen concentration to the dependent variable y_{H_2} (i.e., the mole fraction of hydrogen in the vapor phase). As said earlier, the electrolyte may be supersaturated with hydrogen as found in other gas-evolving electrolysis.[12] Assuming that the ratio of supersaturation to saturation is independent of temperature, this ratio can be lumped with the mass-transfer coefficient, k_m. The temperature dependence of the dissolved hydrogen concentration is incorporated into Eq. 8 by using Henry's law to calculate the mole fraction of dissolved hydrogen at saturation (see assumption 9) as shown below

$$x_{H_2} = \frac{y_{H_2} P}{\mathbf{H}_{H_2}} \quad [9]$$

The Henry s law constant for hydrogen in HF is related to temperature by the following correlation[6]

$$\mathbf{H}_{H_2} = \exp\left(12.26 + \frac{684.97}{T} + 0.969 \ln T\right) \quad [10]$$

According to Eq. 10, the solubility of hydrogen increases with an increase in temperature. Although the solubility of most gases in liquids decreases with temperature, some other systems also show the trend seen in Eq. 10.[13] Substituting Eq. 9 into Eq. 8 results in

$$i_{H_2,a} = \frac{nFk_m}{\mathbf{H}_{H_2}} y_{H_2} P \rho_{m,l} \quad [11]$$

According to Eq. 11, the hydrogen oxidation current is directly proportional to the mass-transfer coefficient, k_m, which incorporates the effect of supersaturation, the partial pressure of hydrogen, and inversely proportional to the Henry s law constant, which decreases with temperature. The current efficiency of the process is equal to the current efficiency of hydrogen generation. Therefore, the overall current efficiency of the reactor is calculated as follows

$$\epsilon = 1 - \frac{w\int_0^L i_{H_2,a} dz}{I} \quad [12]$$

where I is the cell current, and L and w are the length and width, respectively, of the planar electrode (see Fig. 1).

The mole fraction of the fluorochemical (RF) in the vapor phase is related to the mole fraction of hydrogen, the partial pressure of HF in the vapor phase, and the pressure of the vapor phase by the following equilibrium expression derived from experimental measurements

$$\frac{y_{RF}}{y_{H_2}} = 0.82 + 2.44\left(\frac{P - P_{HF}}{P}\right) \quad [13]$$

The above equation is valid in the region of cell operation (pressures from 1.3 to 5.4 atm and temperatures of 10 to 50°C).

Since hydrogen fluoride is the dominant species in the liquid phase, the partial pressure of HF is the same as its vapor pressure and therefore, the mole fraction of HF in vapor phase is given by

$$y_{HF} = \frac{P_{v,HF}(T)}{P} \quad [14]$$

where the HF vapor pressure, $P_{v,HF}$ is related to temperature by the Antoine equation[14]

$$\ln P_{v,HF} = 22.59 - \frac{3404.5}{T + 15.22} \quad [15]$$

Finally, the following constraints are used for the mole fractions of the species in each phase

$$\sum_i y_i = 1 \quad \text{and} \quad \sum_i x_i = 1 \quad [16]$$

To summarize, Eq. 1, 6, 9, 13, 14, and 16 represent the equations needed to relate the five mole fractions and two flow rates in each flow section.

Energy balance.—A steady-state energy balance in each flow section equates the change in enthalpy of the fluid to the rate of electrical work done on the fluid, $\dot{w}_e$, and the energy transferred from the surroundings, $\dot{q}$, as follows

$$\xi\bar{\Delta}\widehat{H}_r + \frac{d(N\widehat{H})}{dz} = \bar{w}_e + q \quad [17]$$

The changes in the kinetic and potential energies along the reactor are negligible compared to enthalpy changes. The enthalpy change of the fluid is composed of two parts: (*i*) energy associated with the heat of the fluorination reaction and (*ii*) energy associated with phase and temperature changes. The fluorination rate per volume, $\dot{\xi}$, is related to the local current density and the hydrogen reoxidation current density by the following expression

$$\dot{\xi} = \frac{(i - i_{H_2})}{2Fd} \quad [18]$$

The specific enthalpy of the two-phase stream, $\hat{H}$, can be related to the mole fractions and specific enthalpies of the individual phases as follows

$$\hat{H} = x_v \hat{H}_v + x_l \hat{H}_l \quad [19]$$

Assuming the enthalpy of mixing to be zero (assumption 6), the enthalpy of the vapor phase ($\hat{H}$) is given by

$$\hat{H}_v = y_{H_2}\hat{H}_{H_2} + y_{RF}\hat{H}_{REv} + y_{HF}\hat{H}_{HEv} \quad [20]$$

Taking the reference state of hydrogen as a gas and that of HF and RF as liquids at 25°C, the specific enthalpy of each species is given by

$$\hat{H}_{H_2} = C_{p,H_2}(T - T_{ref}) \quad [21]$$

$$\hat{H}_{HF,v} = \hat{H}_{HF,l} + \Delta\hat{H}_{vap,HF} \quad [22]$$

$$\hat{H}_{HF,l} = C_{p,HF}(T - T_{ref}) \quad [23]$$

Expressions for the molar enthalpy of the fluorochemical are similar to that for HF. The heat of vaporization for HF is related to the temperature by the following empirical correlation[14]

$$\Delta\hat{H}_{vap,HF} = -82.04 \times 10^3 + 0.50 \times 10^3\, T - 0.52\, T^2 \quad [24]$$

Since HF is the dominant species in the liquid phase, the liquid-phase enthalpy in Eq. 19 is equal to the enthalpy of liquid HF

$$\hat{H}_l = \hat{H}_{HF,l} \quad [25]$$

By assumption 8, the reactor is treated as an adiabatic system and, therefore, $\dot{q}$, is zero in Eq. 17 for all sections of the reactor (see Fig. 1). The rate of electrical work per volume, $\dot{w}_e$, is also zero for all the reactor sections, except the cell pack. In the cell pack, the electrical work done on the fluid in each cell is given by

$$\dot{w}_e = \frac{i\Delta V}{d} \quad [26]$$

where i is the current density and the cell voltage, ΔV, is the voltage drop in each cell of the cell pack. The cell pack voltage is obtained by multiplying ΔV by the total number of cells. The cell voltage has kinetic and ohmic contributions. Experiments conducted on a Simons cell[1] showed that the kinetic contribution was linearly dependent on the current density. Therefore, the cell voltage can be related to the current by

$$\Delta V = (E^\circ + Bi) + \left(\frac{id}{\kappa}\right) \quad [27]$$

where E° is the open-circuit voltage and B is a kinetic constant. Although the cell voltage drop, ΔV, does not vary in the axial direction due to assumption 12, the local current density, i, and the effective conductivity, κ, do vary axially. Therefore, the voltage drop across the cell is coupled to the material, energy, and pressure balances.

The effective conductivity of the electrolyte, κ, is calculated using the bubble-free electrolyte conductivity (κ°) and the volume fraction of the vapor phase (θ_v) by the Bruggeman equation as follows[15]

$$\kappa = \kappa^\circ(1 - \theta_v)^{1.5} \quad [28]$$

The Bruggeman equation should be valid for vapor volume fractions as high as 0.95,[16] as long as the size of the gas bubbles remain an order of magnitude lower than the width of the flow channel.[17] In this study, although the bubbles can span the electrode separation for high vapor fraction cases, the bubble sizes would still be at least two orders of magnitude smaller than the width of the plates.

The volume fraction of the vapor phase (θ_v) is related to the mole fraction and the molar density of the vapor phase, and the average molar density of the two phases by the following equation due to the no-slip condition (see assumption 5)

$$\theta_v = \frac{x_v\rho_m}{\rho_{m,v}} \quad [29]$$

Finally a relationship for the local current density is needed. Although this local current density is not known, the current density integrated over the length of the cell pack is known and is equal to the applied cell current as given below

$$I = w\int_0^L i\,dz \quad [30]$$

Pressure balance.—Due to the effect of pressure on the vapor/liquid equilibrium, the determination of the local pressure is important. The inlet or outlet pressure to the reactor is known, and pressure drops are calculated in order to determine the local pressure in each of the reactor sections. The pressure drop is composed of contributions of the elevation, frictional, and kinetic pressure drops

$$\Delta P = \Delta P_{elevation} + \Delta P_{frictional} + \Delta P_{kinetic} \quad [31]$$

The elevation pressure drop is due to the hydrostatic pressure difference between two points in the reactor, and can be expressed as

$$\Delta P_{elevation} = \rho_{ave} g \Delta z \quad [32]$$

The average fluid density is calculated from contributions from the vapor and liquid phases as

$$\rho_{ave} = (1 - \theta_v)\rho_l + \theta_v\rho_v \quad [33]$$

where the liquid density is known and the ideal gas law is used to calculate the vapor density as follows

$$\rho_v = \frac{P}{RT} MW_v \quad [34]$$

Using assumption 1, and Eq. 16, the average molecular weight of vapor phase can be expressed as

$$MW_v = 2y_{H_2} + MW_{HF}y_{HF} + MW_{RF}y_{RF} \quad [35]$$

where the value of MW_{HF} is 60 g/mol as mentioned in assumption 2.

For one-dimensional, two-phase flow, the pressure drop due to kinetic losses is related to the flow velocity and the average fluid density by the following equation

$$\Delta P_{kinetic} = \Delta(\rho_{ave} v^2) \quad [36]$$

The frictional pressure drop is related to the flow velocity (v), the length of the section (L), hydraulic diameter (D), the effective friction factor (ζ), the contributions of the valves (Δh_i), and entrance and exit effects (e_{vi}) by

$$\Delta P_{frictional} = 0.5\rho_{ave} v^2 \left(\frac{4\zeta\Delta L}{D} + \Sigma\Delta h_i + \Sigma e_{vi}\right) \quad [37]$$

Due to the changes in the flow rate and the shape of the inlet and outlet of the flow distributors, the entrance and exit pressure drops in the distributors are significant. Experiments were conducted at 3M company to obtain the e_{vi} for the geometry of each flow-distributor design.

The effective friction factor, ζ, is a multiple of a Fanning friction factor, f, (which is applicable for single-phase flows), a friction factor multiplier, f', (to account for the effect of two-phase flow), and a constant, K, (which depends on the channel design) and is given as

$$\zeta = Kff' \quad [38]$$

The Fanning friction factor is dependent on the Reynolds number and is calculated differently for laminar flow (i.e., $Re < 2300$) and turbulent flow (i.e., $Re > 2300$). For laminar flow (present in the region near the cell pack entrance), the Hagen-Poiseuille law[18] is used to calculate the friction factor as follows

$$f = \frac{16}{Re} \quad [39]$$

For turbulent flow (present in most of the reactor sections), the Fanning friction factor is calculated using the Blasius equation[18] as follows

$$f = \frac{0.0791}{Re^{0.25}} \quad [40]$$

The Reynolds number is expressed in terms of the liquid density, viscosity, velocity, and the hydraulic diameter for the flow section by

$$Re = \frac{\rho_l v D}{\mu} \quad [41]$$

where the hydraulic diameter is related to the area available for flow and the perimeter wetted by the fluid by

$$D = \frac{4A_{flow}}{S_{flow}} \quad [42]$$

A frictional factor multiplier (f') is used to account for the change in friction factor due to the presence of vapor flow. For a single-phase liquid flow, f' is unity. For vapor volume fractions greater than zero, the following equation obtained by fitting the predictions of Beggs and Brill[19] over the vapor volume fraction range of 0 to 1 is used

$$f' = 1.234 - 0.315 \ln(1 - \theta_v) \quad [43]$$

A summary of the terms used in the governing equations that are not the same for each section of the reactor is shown in Table I.

Solution procedure.—The differential equations used to model the cell pack and the other fluorination reactor sections were solved using the finite-difference method. The differential equations were approximated by three-point difference formulae, and the integrals in Eq. 12 and 30 were approximated by Simpson's rule. The resulting set of algebraic equations was written in Speedup™ (Aspen Technology's equation-based dynamic flowsheet simulator software) and solved using HYBRID, a built-in algebraic equation solver. The solver requires guess values for all the unknown variables. Converged values from a run having a relatively uniform current distribution and low vapor volume fractions were used as guess values for the more nonuniform runs. The solver returns converged values when the tolerances (typically 10^{-10}) were met. The Speedup software is used since it provides: (*i*) a choice of algebraic equation solvers, (*ii*) the ability to extend a steady-state model to a dynamic model taking advantage of the built-in time integrators, (*iii*) a facility to link the various reactor sections among each other and to models of other process units, (*iv*) the ability to interface with user written FORTRAN codes and procedures, and (*v*) the ability to link to Properties Plus,™ Aspen Technology's physical-properties database.

Results and Discussion

The model was used to perform the following tasks

1. Simulate the steady-state profiles of temperature, pressure, vapor volume fraction, and current density in the fluorination reactor to provide insight into the operation of the reactor.

2. Simulate the dependence of the cell pack voltage and current efficiency on the inlet temperature, electrolyte flow rate, and cell current to study the trade-off between power requirements, production rates, and controllability of the reactor.

The values of the physical dimensions and parameters used in the simulations for tasks 1 and 2 are listed in Tables II and III. These values are different from those used in any particular process, but the results are representative of the behavior of a large-scale fluorination reactor.

Profiles of dependent variables in the reactor.—To gain insight into the operation of the fluorination reactor, the profiles of pressure, temperature, vapor volume fraction, and current density are shown in Fig. 2-5, respectively, at two inlet temperatures (27 and 32°C). Fixed values of kinetic constant, B, and mass-transfer coefficient, k_m, were used as their dependence on the operating conditions is not known. The other operating conditions and model parameters used to generate Fig. 2-5 are shown in Tables II-IV. Where possible, the values for the physical constants in Table III are obtained from experimental measurements and published sources.[14,18] Where no information is available, reasonable values were assumed.

A study of the pressure profile (Fig. 2) shows that the pressure drops are steep (ca. 1.5 atm/m) in the outlet and inlet flow distributors and gradual in the rest of the fluorination reactor sections. The pressure gradients are highest in the outlet flow distributors. Entrance and exit effects are also present in the outlet flow distributor, producing a steep

Table I. Summary of the differences in governing equations for different sections.

Section	Term			
	$\dot{w}_e$	$i_{H_2,a}$	$\Sigma\Delta h$	e_{vent}, e_{vexit}
Inlet pipe	0	0	1.8	—
Inlet flow distributor	0	0	0	−0.98,1.40
Cell	Eq. 26	Eq. 8	0	—
Outlet flow distributor	0	0	0	−0.98,1.40
Outlet pipe	0	0	0.55	—

Table II. Physical dimensions of the fluorination reactor sections.[a]

Section	Dimensions			
	Length, L (m)	Width, w (cm)	Inside diameter (cm)	Separation distance, d (cm)
Inlet pipe	0.60	—	30.0	—
Inlet flow distributor	0.15	0.50	—	0.12
Cell[a]	1.50	90.0	—	0.08
Outlet flow distributor	0.15	0.50	—	0.12
Outlet pipe	0.60	—	32.0	—

[a] The cell pack consists of 26 parallel-plate cells, and each of the parallel-plate cells has 18 inlet and outlet flow distributors.

Table III. Physical parameters used in the simulations. The specific heat of HF and hydrogen were obtained from Ref. 14 and 18, respectively. All other values are either assumed or design parameters.

Parameter	Value
Specific heat of HF electrolyte ($C_{p,HF}$)	150 J/mol°C
Specific heat of hydrogen (C_{p,H_2})	29 J/mol°C
Liquid density (ρ_l)	1.12 g/cm^3
Liquid viscosity (μ)	0.8 cp
Mass-transfer coefficient (k_m)	38.4×10^{-3} cm/s
Specific heat of liquid fluorochemical ($C_{p,RF}$)	63 J/mol°C
Heat of vaporization of RF ($\Delta H_{vap,RF}$)	4890 J/mol
Molecular weight of RF	60
Bubble-free solution conductivity (κ°)	0.05 S/cm
Open-circuit potential (E°)	3.0 V
Kinetic voltage constant (B)	20.9 (Ω cm^2)
Heat of reaction (ΔH_r)	193 kJ/mol
Channel frictional constant (K)	1.0

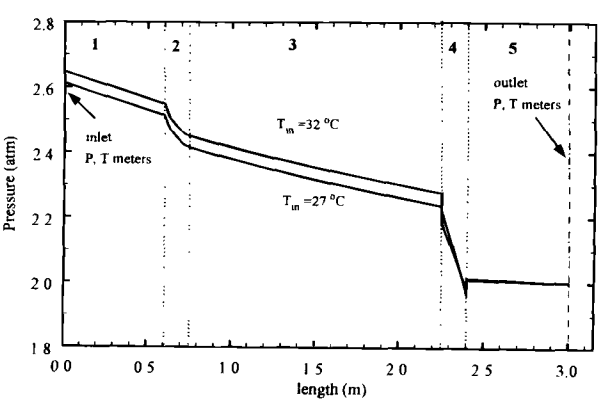

Fig. 2. Pressure profile in the fluorination reactor for inlet temperatures of 27 and 32°C. The other operating conditions are shown in Table IV. The section numbers shown correspond to: 1, inlet pipe; 2, inlet flow distributors; 3, cell pack; 4, outlet flow distributors; and 5, outlet pipe. The locations of pressure and temperature meters are as shown.

Table IV. Operating conditions used in obtaining simulation results presented in Fig. 2-5.

Electrolyte flow rate	6.0 L/s
Cell current	700 A
Outlet pressure	2.0 atm

pressure drop at the entry and a correspondingly steep pressure rise at the exit of the flow distributor. Entrance and exit effects are negligible in other reactor sections. The higher pressure gradients in the flow distributors are due to frictional effects resulting from higher flow velocities. The higher velocities arise from the lower cross-sectional area available for the two-phase fluid flow in the distributors. The pressure drops in all the sections except the flow distributors are mainly composed of the elevation pressure drop (see Eq. 32) because fluid velocities in these sections are low.

Comparison of the pressure profiles at the two inlet temperatures suggests that the pressure gradients in the outlet flow distributors are the most sensitive to the inlet temperature. The sensitivity is due to more vapor generation at higher inlet temperatures resulting in higher fluid velocities and correspondingly higher frictional pressure drops. The change in pressure drop in these distributors affects the local pressure values throughout the cell. Pressure drops in the sections other than the outlet flow distributor do not show an appreciable effect of temperature.

The temperature profiles (see Fig. 3) show that temperatures are constant in the inlet pipe and the inlet flow distributors, rise in the cell pack, drop in the outlet flow distributors, and decrease marginally in the outlet pipe. There is no temperature change in the first two flow sections due to no energy input and the presence of single-phase flow. The temperature increases along the length of the cell pack due to power input. However, the temperature decreases in the outlet flow distributors due to a decrease in pressure leading to the adiabatic evaporation of liquid HF. The temperature decrease in the outlet flow distributors is greater at the higher inlet temperature due to a higher pressure drop as shown in Fig. 2. There is a marginal temperature decrease in the outlet pipe also due to adiabatic vaporization. The use of a higher inlet temperature results in higher temperatures throughout the fluorination reactor. The maximum temperature in the fluorination reactor occurs in the cell pack and can be about 1°C greater than the outlet temperature.

The changes in pressure and temperature affect the vapor volume fractions in each of the fluorination reactor sections as shown in Fig. 4. There is no vapor fraction in the inlet pipe and flow distributors due to a single-phase (liquid) feed and no vapor generation in these sections.

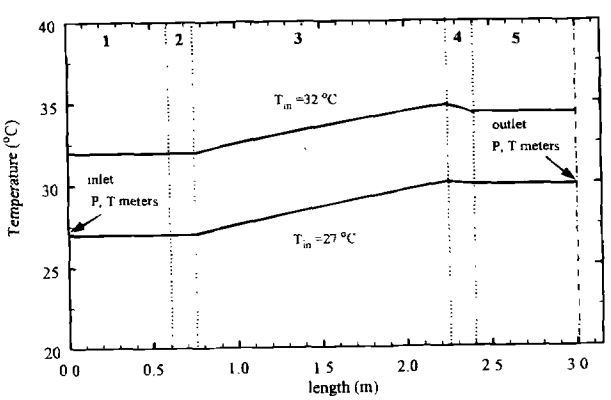

Fig. 3. Temperature profile in the fluorination reactor for inlet temperatures of 27 and 32°C. The other operating conditions are shown in Table IV. The section numbers shown correspond to: 1, inlet pipe; 2, inlet flow distributors; 3, cell pack; 4, outlet flow distributors; and 5, outlet pipe. The locations of pressure and temperature meters are as shown.

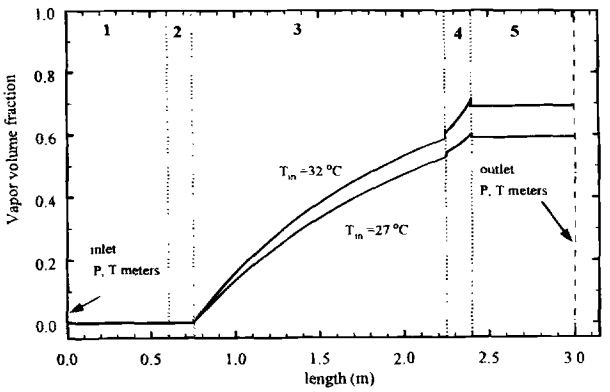

Fig. 4. Vapor volume fraction profile in the fluorination reactor for inlet temperatures of 27 and 32°C. The other operating conditions are shown in Table IV. The section numbers shown correspond as: 1, inlet pipe; 2, inlet flow distributors; 3, cell pack; 4, outlet flow distributors, and 5, outlet pipe. The locations of pressure and temperature meters are as shown.

The vapor fraction increases throughout the cell pack due to hydrogen gas production, which is dependent on cell current and fluorochemical production efficiency. The volume of vapor produced is, however, also dependent on the local pressures and temperatures. A steep rise in the vapor fraction is seen in the outlet flow distributors. It is due to a high pressure drop in the outlet flow distributor as shown earlier (Fig. 2), which leads to a higher volume of the vapor phase. The rise in the vapor fraction is greater at higher inlet temperature due to higher pressure drop in the flow distributor. The vapor fraction increases gradually in the outlet pipe due to a gradual pressure drop in that section.

Figure 5 shows the current density throughout the cell pack at two inlet temperatures. The current in the other regions of the reactor is zero. The plots show that an increase in the inlet temperature results in a less uniform current distribution. This is due to higher vapor fractions at higher temperatures leading to larger ohmic resistances as the fluid progresses up the reactor. Ohmic resistance, however, still contributes less than 10% of the cell voltage even at vapor fractions as high as 0.7. Therefore, even though there is some nonuniformity in the current density due to the variation in the ohmic resistance along the length, the maximum and minimum values of the spatial current density are within 10% of the average value.

Effect of operating conditions on the cell pack voltage and current efficiency.—To study the performance of the reactor and identify problematic operating regions, the cell pack voltage and the current efficiency of the process were calculated over a range of inlet temperatures, flow

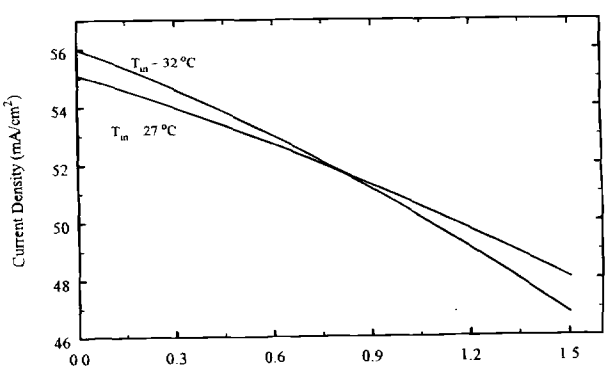

Fig. 5. Current density profiles in the cell pack for inlet temperatures of 27 and 32°C. The cell current is 700 A, which corresponds to an average current density of 52 mA/cm². The other operating conditions are shown in Table IV.

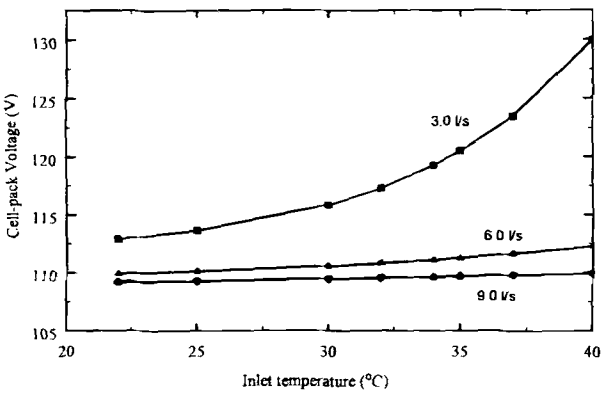

Fig. 6. Cell pack voltage predicted by the model for various inlet temperatures and electrolyte feed flow rates. The other operating conditions are shown in Table IV. The symbols represent discrete simulations, and the lines connect these symbols.

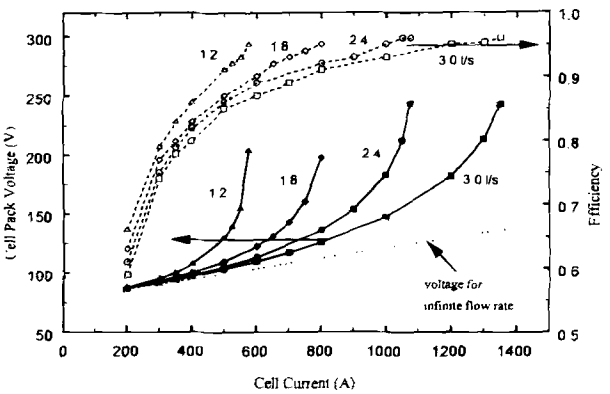

Fig. 8. Cell pack voltage and current efficiency predicted by the model for various cell currents and electrolyte feed flow rates. The inlet temperature and pressure were fixed at 32°C and 2.0 atm, respectively. The symbols represent discrete simulations, and the lines connect these symbols.

rates, and currents (see Fig. 6, 7, and 8, respectively). The cell pack voltages in Fig. 6 and 8 are obtained by multiplying the cell voltage, ΔV, by the number of cells in the cell pack, which is 26 for the results shown here. In Fig. 6 and 7, the cell current and outlet pressure are kept at 700 A and 2.0 atm, respectively. The other model input parameters are listed in Tables II and III. Figure 6 shows that the voltage increases with increasing temperature. The increase is more pronounced at higher temperatures and lower flow rates. For example, at a feed flow rate of 3.0 L/s, a temperature increase from 35 to 40°C results in an increase of approximately 8% in the pack voltage compared to only a 2% increase when the temperature increases from 25 to 30°C. The sensitivity of voltage to temperature is less pronounced at high flow rates. For example, at 9.0 L/s, a temperature increase from 35 to 40°C results in only a 0.3% increase in the voltage. The sensitivity of voltage to temperature and flow rate can be attributed to a corresponding sensitivity in the vapor volume fraction. At 3.0 L/s, a temperature increase from 35 to 40°C increases the vapor volume fraction from 0.85 to 0.90. The same temperature increase at 9.0 L/s increases the vapor fraction from 0.45 to 0.50 only. At lower flow rates, more evaporation occurs since the residence time of the fluid is larger. The resultant increase in the vapor fraction leads to lower conductivities, which results in larger cell voltages. The model may overpredict the vapor fractions at values greater than 0.6 due to the no-slip limitation. Therefore, the voltages resulting from the high vapor fractions can be viewed as an upper bound.

As seen in Fig. 7, the current efficiency also increases with temperature and decreases with flow rate. At 3.0 L/s

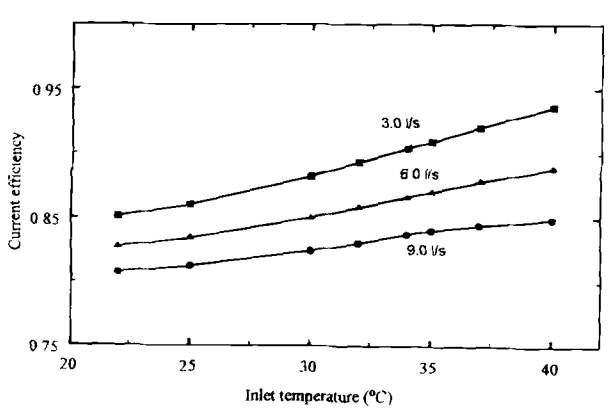

Fig. 7. Current efficiency predicted by the model for various inlet temperatures and electrolyte feed flow rates. The other operating conditions are shown in Table IV. The symbols represent discrete simulations, and the lines connect these symbols.

the efficiency increases by about 6% as the temperature increases from 25 to 35°C. The increase in current efficiency with temperature (i.e., a decrease in hydrogen oxidation current) is due to lower dissolved hydrogen concentrations (see Eq. 8). This appears contradictory to Eq. 10, which indicates that the Henry's law constant decreases, and hence the mole fraction in the vapor phase (i.e., decrease in y_{H_2}). The reduced hydrogen partial pressure results in lower dissolved hydrogen and, therefore, higher efficiency in spite of the increase in hydrogen solubility with temperature. Similarly, lower flow rates result in larger efficiencies because of lower cell pressures for a fixed outlet pressure. Lower cell pressures mean lower hydrogen partial pressures, and consequently lower hydrogen oxidation currents.

In order to summarize the cell performance over a range of operating conditions, the cell pack voltage and current efficiency are plotted in Fig. 8 as a function of cell current and electrolyte flow rate. The inlet temperature and outlet pressure are fixed at 32°C and 2.0 atm, respectively, and the other model input parameters are listed in Tables II and III. As shown in Fig. 8, at low currents the cell pack voltage increases linearly with current. Further increases in current cause the cell pack voltage to change into an exponential voltage rise. The current at which this transition occurs increases with flow rate. The vapor fractions in the cell increase at higher cell currents and lower flows resulting in lower electrolyte conductivity and larger ohmic drops. The cell voltage which is composed of kinetic and ohmic contributions (see Eq. 27), rises steeply when the ohmic contribution becomes significant.

To understand better the effect of vapor fractions on the voltage, the cell pack voltage for the case of infinite flow rate is also shown in Fig. 8 by a dotted line. At an infinite flow rate, the vapor in the cell is negligible, and the conductivity, κ, is equal to the conductivity of the bubble-free electrolyte, κ°, throughout the cell. Therefore, the current distribution is uniform, and the cell voltage vs. applied current can be obtained directly from Eq. 27 by substituting the current density, i, by I_{cell}/Lw. The dotted line representing the case for infinite flow rate is shown on Fig. 8 for two reasons. First, the deviation of the solid lines from the dotted line shows the extent to which the vapor contributes to the cell voltage. Second, it enables one to see the sensitivity of the kinetic parameter B on the cell voltage more easily.

The value of the cell current where the vapor contributes significantly to the voltage is flow-rate dependent. For example, at flow rates of 1.2 and 3.0 L/s, the solid line is approximately 30% greater than the dotted line at 500 and 1100 A, respectively. As the voltage deviates from the solid line by more than 30%, the voltage begins to increase exponentially with current. The exponential rise in cell pack

voltage with current may lead to operational instabilities since small current fluctuations lead to large voltage fluctuations. Large cell voltages may also lead to a short circuit in the reactor since most of the current is forced to a very small region near the entrance to the cell pack resulting in extremely high current densities. Although not shown in the figure, the overall pressure drop in the reactor shows a profile similar to the cell pack voltage shown in Fig. 8 due to an increase in the frictional pressure drop as the vapor fraction increases. Large fluctuations in the pressure may also lead to operational instabilities.

Although the current at which the solid lines deviate from the dotted line by 30% increases with flow rate, the amount of energy added for every liter of feed is approximately constant at 50 kJ/L at each transition point. The simulations show that this ratio translates into evaporation of 5% of the total moles entering the cell, leading to approximately 90% of the cell volume being occupied by vapor. This observation may be used to establish the following rule of thumb: the current and flow rate must be balanced such that the feed evaporated by the input energy does not occupy more than 90% of the cell volume. The operating current needed to attain the 90% limit may increase if slip between vapor and liquid phases is significant. Qualitatively though, excess vapor in the reactor will most likely lead to operational problems.

The value of B used in the simulations will quantitatively affect the cell pack voltage shown in Fig. 8. As stated above, the dotted line in Fig. 8 (i.e., the case of infinite flow rate) is used to discuss the sensitivity of the kinetic parameter B on the cell voltage. For example, doubling the value of B in Eq. 27 approximately doubles the slope of the dotted line since $B = 20.9\ \Omega\ cm^2$ is 13 times greater than $(d/\kappa^\circ) = 1.6\ \Omega\ cm^2$. However, since the open-circuit potential, E°, is 3.0 V and is the major component of the cell voltage, doubling B at 700 A (51.8 mA/cm^2) increases the cell pack voltage from 108 V to only 136 V (a 26% increase). For finite flow rates, the sensitivity of the voltage to B is similar to that for infinite flow rates. At 3.0 L/s and 700 A, $(d/\kappa) = 7.9\ \Omega\ cm^2$. Doubling B also increases (d/κ) to 10.2 Ω cm^2 due to the additional vapor formed by increasing the energy input. Consequently, the voltage increases from 117 to 147 V, also a 26% increase. For finite flow rates, changing B changes both the kinetic and ohmic resistance. However, the percent change in the cell voltage is similar for both finite and infinite flows.

The efficiency curves in Fig. 8 show a rise in efficiency with increasing cell current. The higher temperatures at higher currents lead to more evaporation of HF and, therefore, a lower hydrogen partial pressure. The lower hydrogen partial pressure results in less dissolved hydrogen concentrations and lower hydrogen oxidation current. A lower hydrogen oxidation current coupled to a higher applied currents results in a significant drop in the fraction of current going into hydrogen oxidation (i.e., higher efficiencies).

The efficiencies shown in Fig. 8 depend on the value of k_m used in the simulations. Although changing k_m indirectly affects a variety of dependent variables (e.g., P and y_{H_2}), it directly affects the hydrogen oxidation current through Eq. 11. Therefore, doubling k_m effectively doubles $i_{H_2,a}$. For example, at 3.0 L/s and 400 A, the efficiency is approximately 0.8, meaning that the hydrogen oxidation current consumes 20% of the cell current. Doubling k_m approximately doubles the hydrogen oxidation current, which reduces the efficiency from approximately 0.8 to 0.6. Lower efficiencies lead to less vapor, which in turn decreases the voltage. However, low efficiencies occur at low currents where the vapor has a small affect on the voltage. At high currents, where the voltage is sensitive to the amount of vapor present in the reactor, the efficiencies are high. Therefore, even though the value of k_m used to generate Fig. 8 will affect the predicted efficiencies at low currents, it will have a negligible affect on the cell pack voltage over the whole range of currents.

The possible operational problems discussed in relation to Fig. 8 can be further appreciated when examining the

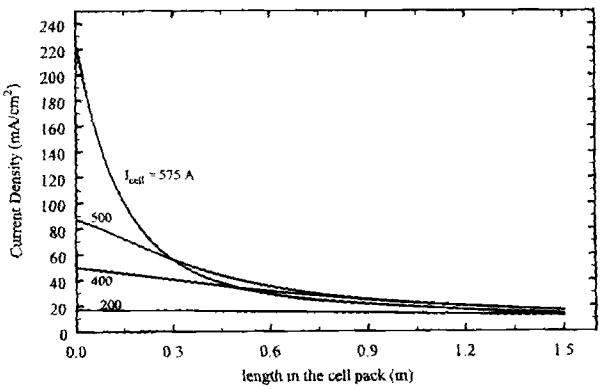

Fig. 9. Current density profiles in the cell pack for a flow rate of 1.2 L/s at different cell currents. Based on an electrode area of 1.35 m², the overall average current density for 200, 400, 500, and 575 A is 14.8, 29.6, 37.0, and 42.6 mA/cm², respectively. The inlet temperature and pressure were fixed at 32°C and 2.0 atm, respectively.

current distribution in the cell. The effect of applied current on the current distribution in the cell is shown in Fig. 9. The profiles are plotted for four cell currents at a flow rate of 1.2 L/s. An increase in the current from 200 to 400 A results in a moderate redistribution of the current and a corresponding rise in the cell pack voltage from 88 to 107 V (see Fig. 8). At 400 A, the current density at the entrance to the cell pack is 1.7 times larger than the overall current density of 37 mA/cm^2. However, increasing the current further 500 and 575 A causes the cell pack voltage to rise to 129 and 204 V, respectively. In the later cases, the current density becomes very nonuniform due to high ohmic resistances at large vapor volume fractions. At 575 A, the current density at the entrance to the cell pack is 5.5 times larger than the overall average of 43 mA/cm^2. These high local current densities may lead to short-circuiting of the cell pack via excessive shunt-current or via electric arc formation between the electrodes.

From a production standpoint, it is desirable to operate a cell at high efficiencies and high currents in order to maximize production. In typical electrochemical reactors (e.g., electrowinning of metals[20] or reduction of nitrates and nitrites,[21]) higher currents usually result in lower efficiencies due to competing reactions. In these cases, a trade-off must be made between cell current and efficiency to optimize the production rate. For the bipolar forced-flow, fluorination reactor, higher currents always lead to a higher production rates since the current efficiency con-

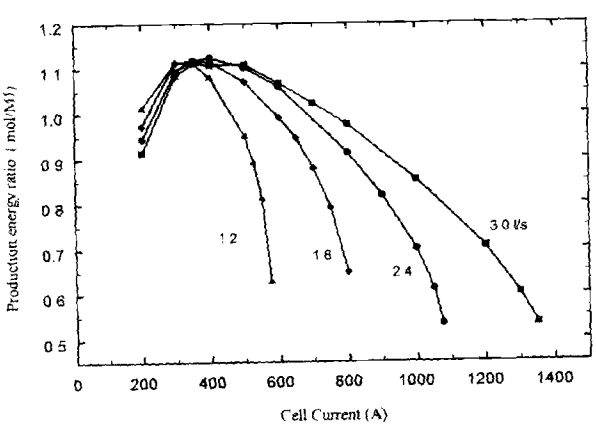

Fig. 10. Production/energy ration predicted by the model for various cell currents and electrolyte feed flow rates. The inlet temperature and pressure were fixed at 32°C and 2.0 atm, respectively. The symbols represent discrete simulations, and the lines connect these symbols.

tinuously increases. The high production rates, however, require more energy. The trade-off between production rates and power input is shown in Fig. 10 as a function of current and flow rate. The ordinate in Fig. 10, labeled production/energy ratio, is obtained by dividing the fluorochemical production rate (proportional to ϵI) by the power input ($I\Delta V$). For the cell design and operating conditions used in this study, the production/energy ratio shows a maximum at a current of approximately 350 A for all four flow rates. The maximum in the production/energy ratio is not sensitive to the flow rate due to the relative insensitivity of efficiency and voltage to flow rate at low currents (see Fig. 8). Below 350 A, the cell voltage is dominated by kinetic resistance, which is relatively flow insensitive. However, at high currents, and presumably very low flows, the ohmic resistance dominates due to a large vapor volume fraction in the cell. At large vapor fractions, the cell voltage, and consequently the power input, is very sensitive to the flow rate.

A maximum is obtained for the production/energy ratio because, at low currents, the percentage increase in efficiency is more than that for the cell voltage. At currents higher than 350 A, the percentage increase in cell voltage becomes greater than that for the current efficiency and, therefore, the production/energy ratio decreases. A cell current of 350 A would give an optimum operating current from the standpoint of production rate and energy input. However, the selling cost of fluorochemical and cost of the electrical power need to be considered to obtain the economic optimum current. For a high-value fluorochemical, it may be profitable to operate the reactor at the currents above the maximum seen in Fig. 10. Care must be taken though in operating the reactor at high currents. For example, Fig. 8 indicates that controlling the cell at currents above 500 A at a flow rate of 1.2 L/s may be difficult. Small current fluctuations lead to large voltage swings, which may cause severe operational problems and ultimately short-circuiting.

Conclusions

A mathematical model of a parallel-plate fluorination reactor was developed. Profiles of pressure, temperature, and vapor volume fraction throughout the fluorination reactor were presented to gain insight into the operation of the reactor. The profiles show that the cell pack and the flow distributors, especially the outlet flow distributors, have significant effects on the operation of the fluorination reactor. These effects become greater at higher inlet temperatures. A study of the effect of temperature on the local current-density profiles in the cell pack showed that higher inlet temperatures lead to a less uniform current distribution due to higher vapor volume fractions. The effect of feed flow rate, inlet temperature, and cell current on the cell pack voltage and current efficiency were also studied. While higher temperatures, higher currents, and lower feed rates lead to a higher current efficiency, they also lead to higher cell pack voltages and power input. Also, while higher currents lead to higher production rates, care should be taken not to operate the reactor in a region where small current fluctuations may lead to large voltage swings. As a rule of thumb for safe reactor operation, the current and flow rate must be balanced such that the feed evaporated by the input energy does not occupy more than 90% of the cell volume.

Acknowledgment

This work was made possible by financial support from 3M Company.

Manuscript submitted February 9, 1998; revised manuscript received May 28, 1998.

The University of South Carolina assisted in meeting the publication costs of this article.

LIST OF SYMBOLS

A_{flow} cross-sectional area for flow, cm^2
B kinetic parameter used in Eq. 27, $\Omega\ cm^2$
C_{b,H_2} bulk concentration of dissolved hydrogen, mol/cm^3
$C_{p,k}$ specific heat of species k, J/mol-°C
d separation gap between the plates in the cell pack, cm
D hydraulic diameter, cm
$e_{v,i}$ entrance and exit pressure drop factor for flow distributor
E° open-circuit potential, V
f fanning friction factor
f' frictional factor multiplier
F Faraday's constant, 96,487 C/equiv
g gravitational acceleration, 981 cm/s^2
Δh_i contributions of the valves to pressure drop in section, i, of the reactor (see Eq. 37)
$\hat{H}$ average molar enthalpy of the two-phase mixture, J/mol
$\hat{H}_l$ liquid molar enthalpy, J/mol
$\hat{H}_v$ vapor molar enthalpy, J/mol
$\hat{H}_i$ molar enthalpy of species i, J/mol
$\hat{H}_{i,l}$ molar enthalpy of species i in liquid phase, J/mol
$\hat{H}_{i,v}$ molar enthalpy of species i in vapor phase, J/mol
$\mathbf{H}_{H_2}$ Henry's law constant for hydrogen, Pa
ΔH_r heat of reaction, J/mol
$\Delta H_{vap,i}$ heat of vaporization of species i, J/mol
i local current density, A/cm^2
$i_{H_2,a}$ hydrogen oxidation current, A/cm^2
I cell current, A
k_m mass-transfer coefficient for dissolved hydrogen, cm/s
K channel frictional constant
L length of each electrode in the cell pack, cm
MW_l average molecular weight of the liquid phase, g/mol
MW_v average molecular weight of the vapor phase, g/mol
n number of electrons taking part in hydrogen evolution reaction
$\dot{N}$ average molar flux of the two-phase mixture, mol/cm^2-s
N_{H_2} flux of hydrogen in vapor phase, mol/cm^2-s
P total pressure, $g/cm\cdot s^2$
P_{HF} partial pressure of HF in vapor phase, $g/cm\cdot s^2$
P_{vHF} vapor pressure of hydrogen fluoride, $g/cm\cdot s^2$
ΔP_{elev} pressure drop due to elevation change, $g/cm\cdot s^2$
ΔP_{fr} pressure drop due to frictional losses, $g/cm\cdot s^2$
ΔP_{kin} pressure drop due to kinetic losses, $g/cm\cdot s^2$
$\dot{q}$ rate of heat transfer, W/cm^3
$\dot{Q}$ inlet volumetric flow rate, cm^3/s
R gas constant, 8.314 J/mol-K
Re Reynolds number
S_{flow} perimeter wetted by flow, cm
t time, s
T temperature, K
v average flow velocity of the two-phase mixture, cm/s
ΔV voltage drop per cell, V
w width of the planar electrodes in the cell pack, cm
$\dot{w}_e$ electrical power density, W/cm^3
x_{H_2} mole fraction of hydrogen in liquid phase
x_l moles of liquid per mole of two-phase mixture
x_v moles of vapor per mole of two-phase mixture
y_i mole fraction of species i in vapor phase
z axial distance in the reactor, cm

Greek

ϵ current efficiency
κ effective conductivity of the electrolyte, $\Omega^{-1}\ cm^{-1}$
κ° conductivity of bubble-free electrolyte, $\Omega^{-1}\ cm^{-1}$
θ_v vapor volume fraction
ρ_{ave} average mass density of the two-phase mixture, g/cm^3
ρ_l mass density of the liquid phase, g/cm^3
ρ_v mass density of the vapor phase, g/cm^3
ρ_m average molar density of the two-phase mixture, mol/cm^3
$\rho_{m,l}$ molar density of the liquid phase, mol/cm^3
$\rho_{m,v}$ molar density of the vapor phase, mol/cm^3
ζ effective friction factor
$\dot{\xi}$ reaction rate, mol/s
μ viscosity of the electrolyte, g/cm·s

Subscripts

ave average
HF oligomerized HF
H_2 hydrogen
l liquid
RF fluorochemical product
v vapor

REFERENCES

1. J. H. Simons, in *Fluorine Chemistry*, J. Simons, Editor, p. 414, Academic Press, New York (1950).
2. W. V. Childs, F. W. Klink, J. C. Smeltzer, and J. C. Spangler, U.S. Pat. 5,322,597 (1994).
3. K. Jha, J. W. Weidner, and G. L. Bauer, in *Proceedings of the Symposium on Electrochemistry in the Preparation of Fluorine and Its Compounds*, W. V. Childs and T. Fuchigami, Editors, PV 97-15, p. 22, The Electrochemcial Society Proceeding Series, Pennington, NJ (1997).
4. J. A. Drake, J. Newman, and C. J. Radke, *J. Electrochem. Soc.*, **145**, 1578 (1998).
5. W. Schotte, *Ind. Eng. Chem. Res.*, **26**, 300 (1987).
6. *Aspen Plus Database 9.3*, Aspen Technology, Cambridge, MA (1996).
7. M. Ali, M. Sadatomi, and M. Kawaji, *Can. J. Chem. Eng.*, **71**, 657 (1993).
8. G. Wallis, *One-Dimensional Two-Phase Flow*, McGraw-Hill, New York (1969).
9. J. E. Funk and J. F. Thorpe, *J. Electrochem. Soc.*, **116**, 48 (1969).
10. Y. Nishiki, K. Aoki, K. Tokuda, and H. Matsuda, *J. Appl. Electrochem.*, **16**, 615 (1986).
11. J. F. Yan, P. S. Fedkiw, and C. G. Law, *J. Appl. Electrochem.*, **26**, 175 (1996).
12. H. Vogt, in *Comprehensive Treatise of Electrochemistry*, Vol. 6, J. O'M. Bockris, B. E. Conway, and S. Sarangapani, Editors, Plenum Press, New York (1983).
13. R. Reid, J. Prausnitz, and B. Poling, *The Properties of Gases and Liquids*, 4th ed., p. 332, McGraw-Hill Company, New York (1986).
14. *Matheson Gas Databook*, 6th ed., Matheson Gas Products, East Rutherford, NJ (1980).
15. D. Bruggeman, *Ann. Phys.*, **24**, 636 (1935).
16. P. J. Sides, in *Modern Aspects of Electrochemistry*, Vol. 18, R. E. White, J. M. Bockris, and B. E. Conway, Editors, Plenum Press, New York (1986).
17. P. J. Sides, Ph.D. Thesis. University of California, Berkeley, CA (1981).
18. R. Perry and D. Green, *Chemical Engineers Handbook*, 6th ed., McGraw-Hill Book Company, New York (1984).
19. H. Beggs, and J. Brill, *J. Pet. Technol.*, 607 (May 1973).
20. M. E. El-Shakre, M. M. Saleh, B. E. El-Anadouli, and B. G. Ateya, *J. Electrochem. Soc.*, **141**, 441 (1994).
21. S. Prasad, J. W. Weidner, and A. E. Farell, *J. Electrochem. Soc.*, **142**, 3815 (1995).

Effect of Temperature on the Voltammetric Behavior of Poly-*o*-toluidine

M. I. Florit and D. Posadas

Instituto de Investigaciones Fisicoquímicas Teóricas y Aplicadas, Departamento de Química, Facultad de Ciencias Exactas, Universidad Nacional de la Plata, 1900 La Plata, Argentina

F. V. Molina

Instituto de Química del Medio Ambiente y Energía, Departamento de Química Inorgánica, Analítica y Química Física, Facultad de Ciencias Exactas y Naturales, Ciudad Universitaria, Buenos Aires 1428, Argentina

ABSTRACT

The voltammetric response of poly(*o*-toluidine) electrochemically grown films of about 62 nm thick was investigated in the temperature range 218–293 K, using 3.7 M sulfuric acid. The peak current, i_p, corresponding to the first oxidation process decreases with temperature. The peak current depends linearly on the sweep rate at all temperatures. At about 260–270 K, a discontinuity in the i_p vs. T plot is observed. The peak potential for the anodic sweep shifts in the positive direction as the temperature is decreased and the full peak width at half-maximum, E_w, increases as temperature is decreased. On the other hand, for the cathodic sweep, the peak potential just slightly shifts in the positive direction, and E_w does not change as the temperature is decreased. In strongly acidic H_2SO_4 solutions, the voltammetric capacity, $i_p v^{-1}$, is found to be dependent on anion concentration rather than on pH. The temperature dependence of the voltammetric response is explained on the basis that the oxidation process is controlled by ionic movements into the polymer. As the temperature decreases, ionic movements become hindered and a decrease of the polymer voltammetric capacitive current, associated to the redox process, occurs.

Introduction

Poly(aniline) (PANI) and other polymers derived from substituted aromatic amines have aroused much interest because of their many potential applications. Although the voltammetric behavior of these polymers has been widely studied (see Ref. 1-5 and references therein) its redox mechanism is not yet well understood.

Moreover, studies of the temperature effect, on a wide temperature range, on the electrochemical behavior of PANI and related polymers are scarce.[5-10] Inzelt[5] studied the temperature dependence of the voltammetric response of PANI film electrodes, in the ranges 273–333 K and 230–276 K, in aqueous and nonaqueous media, respectively. He concludes that the charge transport rate is fast, even at low temperatures, and that the change in the pK_a values of the redox sites with temperature could be the responsible for the shifts observed of the peak potentials. Previously, Gholamian et al.[6] had studied, at room temperature, the resistivity and electrochemical behavior of PANI films synthesized electrochemically at different temperatures. They found an improvement in the conductivity of the films that had been obtained at low temperatures and attributed this finding to a more homogenous polymer structure.

Also, Vuki et al.[7,8] studied the temperature dependence of the redox switching properties of PANI with potentiostatic pulses and very fast voltammetric scans. They found that the charge diminishes with T, and they gave two alternative explanations for their findings: (*i*) the leuco form is less protonated at low T than at room temperature and, (*ii*) the protonation of the leuco form is independent of T and the oxidation rate is being controlled by the slower ingress of anions at low T. On the other hand, Heinze et al.[9,10] studied the reduction of oxidized PANI films in liquid NH_3, interpreting their results in terms of structural changes in the polymer chain upon redox processes.

Besides $HClO_4 \cdot 5.5\ H_2O$, the eutectic acid solution, 3.7 M H_2SO_4, allows performance of electrochemical experiments at temperatures as low as 178 K, even with the electrolyte frozen.[11] Note that the structure of bulk 3.7 M H_2SO_4 is con-